J. Fluid Mech. (2024), *vol*. 996, A7, doi:10.1017/jfm.2024.790

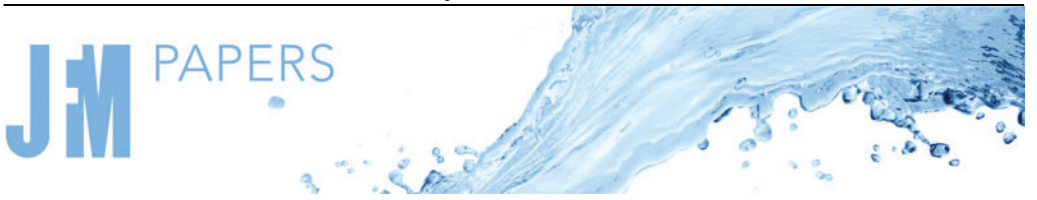

Scaling of vertical coherence and logarithmic energy profile for wall-attached eddies during sand and dust storms

Xuebo Li[1,2,†], **Lan Hu**[1], **Xin Hu**[1] **and Wanting Liu**[3]

[1]School of Science, Chongqing University of Technology, Chongqing 400054, PR China

[2]Center of Spatio-temporal Big Data Research, Chongqing University of Technology, Chongqing 400054, PR China

[3]School of Aerospace Engineering, Huazhong University of Science and Technology, Wuhan 430074, PR China

(Received 15 August 2023; revised 30 April 2024; accepted 6 June 2024)

High-frequency observation data, including all three components of instantaneous fluctuating velocity, temperature, as well as particulate matter 10 (PM_{10}), collected from the unstable atmospheric surface layer at $z/L = -0.11$ and -0.12, L being the Obukhov length, during sand and dust storms (SDS), were used to explore the scaling of vertical coherence and the logarithmic energy profile for wall-attached eddies. The present results demonstrate good agreement with the self-similar range of the wall-attached features for velocity and temperature components, as well as for PM_{10} at lower heights ($z < 15$ m) during SDS. Following the idea depicted by Davenport (*Q. J. R. Meteorol.*, vol. 372, 1961, pp. 194–211), an empirically derived transfer kernel comprises implicit filtering via a scale-dependent gain and phase, parametrically defined as $|H_L^2(f)| = \exp(c_1 - c_2\delta/\lambda_x)$, where c_1 and c_2 are parameters, δ is the boundary layer thickness and λ_x is the streamwise wavelength. Linear coherence spectrum analysis is applied as a filter to separate the coherent and incoherent portions. After this separation procedure, the turbulence intensity decay for wall-attached eddies is described in a log–linear manner, which also identifies how the scaling parameter differs between the measured components. These findings present abundant features of wall-attached eddies during SDS which further are used to improve/enrich existing near-wall models.

Key words: boundary layer structure, buoyant boundary layers, atmospheric flows

† Email address for correspondence: lixuebo.china@gmail.com

1. Introduction

Wind transport of sand and dust is a potent erosional force that generates sand dunes and ripples while also filling the sky with suspended dust aerosols. These phenomena can inflict damage to infrastructures, telecommunications and crops, impacting transportation due to reduced visibility and resulting in significant economic losses (Sivakumar 2005; Middleton & Kang 2017; Song *et al.* 2022; Liu *et al.* 2023). Therefore, acquiring a comprehensive understanding of the mechanisms behind sand and dust storms (SDS) is essential, where turbulent structures play a dominant role in the transportation of sand and dust. The SDS interact intricately with other non-turbulent motions including gravity waves, solitary waves and low-level jets (Terradellas *et al.* 2005; Banta, Pichugina & Brewer 2006; Sun *et al.* 2015). As such, gaining insights into these turbulent features becomes paramount in delving further into the intricate dynamics of SDS. The effect of particles on the coherent structure evolution depends on various factors, including both particle and flow parameters. Due to the complexity of the multiphase flow rather than the single-phase flow, it remains to reach a consensus on the particle effects if only the streamwise vortices are investigated. For example, different influences on the turbulence size and inclination angle are observed under different scenarios (Dritselis & Vlachos 2008, 2011; Zhao, Andersson & Gillissen 2010; Li *et al.* 2012). However, the scarcity of multiheight and high-frequency wind and dust data presents a challenge in comprehensively studying the dynamic properties of SDS (Akhlaq, Sheltami & Mouftah 2012; Albarakat & Lakshmi 2019; Li *et al.* 2021*a*). The challenge particularly applies to understanding interactions between flow and dust fields, along with the characteristics of coherent structures. This study aims to address these challenges regarding the turbulent models and multiheight interactions in detail, building upon unique observations from the atmospheric surface layer (ASL).

Flow structures with a hierarchical ordering of scales in the wall-normal direction, considerable lifetimes in the streamwise direction and arrangements in both the spanwise and streamwise directions have been employed to demonstrate large-scale coherence in high Reynolds number wall turbulence (Favre, Gaviglio & Dumas 1967; Wark & Nagib 1991; Ganapathisubramani, Longmire & Marusic 2003; Tomkins & Adrian 2003; Hutchins & Marusic 2007; Baars, Hutchins & Marusic 2017). This large-scale flow structure is most visible in the logarithmic region of the turbulent boundary layer (TBL), where turbulent kinetic energy (TKE) is mostly composed of large-scale energy (Hutchins & Marusic 2007). These coherent structures range in scale from the extent of the very large-scale motions (extending up to 10δ in the streamwise direction, where δ is the boundary layer thickness (Salesky & Anderson 2020)) down to the viscosity scale (ν/u_τ, where ν is the kinetic viscosity, and u_τ is the friction velocity), which represents the smallest scale of turbulence. A thorough reading on coherent structures in laboratory flows can be found in the reviews of Robinson (1991) and Jiménez (2018). The attached eddy hypothesis (AEH) is a theoretical framework for wall-bounded flow that idealizes wall-bounded flow as a set of inertia-driven coherent structures, which are self-similar and randomly scattered in the plane of the wall (Townsend 1976). A recent description by Marusic & Monty (2019) explains the basic assumptions and constraints of AEH. According to Perry & Chong (1982), these coherent formations, or eddies, scale with the distance from the wall, and the height of the eddies follows a geometric evolution based on AEH. Evidence in favour of self-similarity and wall-scaling has been published by the boundary layer community (e.g. Jiménez 2012; Hwang 2015; Baars *et al.* 2017; Marusic, Baars & Hutchins 2017). Results from Del Alamo *et al.* (2006) characterize for the first time the structural organization of the self-similar range of the turbulent

logarithmic region. The extraction of instantaneous structures, analysis of their self-similar characteristics and scaling laws of statistics are also well-presented. Lozano-Durán & Jiménez (2014) discovered that these eddies grow large, attach to the wall, extend across the logarithmic layer and exhibit geometric and temporal self-similarity, with lifetimes proportional to their size (or distance from the wall). These structures also explain the previously observed symmetry between sweeps and ejections (Lozano-Durán, Flores & Jiménez 2012). Hwang & Sung (2018) characterized the AEH as offering a 'unified theory for the asymptotic behaviours of wall turbulence'. Further research by Hwang & Sung (2019) revealed that the identified coherent structures are directly connected to the logarithmic velocity law and serve as the structural basis for the inertial layer. In addition to the basis of AEH, Marusic *et al.* (2010) developed a mathematical model to forecast near-wall turbulence given just large-scale knowledge from the outer boundary layer area. This model has been extended to a refined inner–outer interaction model based on spectral stochastic estimation of turbulence by Baars, Hutchins & Marusic (2016). Further, Baars *et al.* (2016) proposed an empirically derived transfer kernel comprising implicit filtering via a scale-dependent gain and phase to capture the coherent portion in the prediction. Inspired by the interactions between near-wall and outer boundary layer regions, we aim to extend the AEH model to describe vertical coherence, thereby exploring coherence features during SDS.

Baars *et al.* (2017) investigated two-point measurements in the wall-normal direction in smooth terrain with well-controlled flow circumstances, where the novel set-up allowed researchers to explore the relationship between outer-region turbulence and the near-wall footprint in the fluctuating velocity spanning a friction Reynolds number range $Re_\tau \sim O(10^3)$–$O(10^6)$. They further showed that the self-similarity in the neutral laboratory zero-pressure gradient TBL is characterized by a streamwise/wall-normal aspect ratio of $AR = \lambda_x/\Delta z \approx 14$, which was also investigated by Duan *et al.* (2020) in channel flows. Baidya *et al.* (2019) reported that the self-similar wall-attached structures follow a three-dimensional aspect ratio of $14 : 1 : 1$ in the streamwise, spanwise and wall-normal directions in high Reynolds number pipe and boundary layer flows. In addition, both Krug *et al.* (2019) and Li *et al.* (2022*a*) explored the coherence for both velocity and temperature signals in the ASL. They found that the streamwise/wall-normal aspect ratio decays with a logarithmic trend with increasing unstable thermal stratification. More recently, Basley, Perret & Mathis (2019) and Li, Wang & Zheng (2022*b*) explored the wall similarity under roughness surface in laboratory and atmospheric observations, giving that the aspect ratio of coherent structures increases with increasing surface roughness. Previous studies by Zhang, Hu & Zheng (2018) and Wang, Gu & Zheng (2020) have shown that the dust field possesses similar coherent structures to the fluid field. Given that dust particles adhere to the flow field and share similar structures, the remaining unknown similarity features of aspect ratio for dust field during SDS are identified specifically in the current study.

One of the goals of analysing AEH flow data is to look for scaling laws in the energy spectra (Nickels *et al.* 2005; Baidya *et al.* 2017) and wall-normal profiles of turbulent stresses (Marusic *et al.* 2013). The population density of linked eddies is inversely proportional to their height (H), which fluctuates in the range $O(z_{min}) \leq H \leq O(\delta)$, where z_{min} marks the start of the inertial region. The cumulative contribution from the spectrum of linked eddies causes the streamwise turbulence intensities to differ logarithmically as a function of z at any $z \geq z_{min}$. This structure is also illustrated by the semilogarithmic wall-normal decay of the variance of the streamwise velocity. This scaling has already been observed by simulations, experimental investigations and other theoretical arguments (Perry & Abell 1977; Perry, Henbest & Chong 1986; Nikora

1999; Katul, Porporato & Nikora 2012; Li, Wang & Zheng 2021*b*). In addition to low Reynolds number simulations (Jiménez & Hoyas 2008; Lee & Moser 2015), experimental datasets (Hultmark *et al.* 2012; Marusic *et al.* 2013) and atmospheric observations (Kunkel & Marusic 2006; Krug *et al.* 2019; Li *et al.* 2022*a*) at high Reynolds numbers have indicated that self-similar contributions at the same scale are veiled by non-self-similar contributions, implying that a logarithmic law for $\overline{u^2}^+$ (the symbol $()^+$ indicates wall units) is more persuasive (Rosenberg *et al.* 2013; Baars & Marusic 2020*b*). Notably, Baars & Marusic (2020*b*) separated these two contributions (self-similar and non-self-similar), exposing the near-wall logarithmic growth (of $\overline{u^2}^+$) down to $z^+ \sim 80$, where the lower bound was reported by Duan *et al.* (2020) at $z^+ \sim 100$ with a slope of 0.98 ($= A_1$). The slope of the logarithmic variation of the streamwise variance in wall turbulence is the Townsend–Perry constant (Marusic *et al.* 2013; Baars & Marusic 2020*b*). Considering the hierarchy of geometrically self-similar eddy motions that expand through wall-normal separation featuring a logarithmic energy contribution, and a reference point that has been fixed at a near-wall region previously to obtain the wall-attached eddies along all three axis directions, we postulate that self-similar eddies also feature a logarithmic energy distribution during the SDS for components of velocity, temperature and PM_{10}. The above review readily demonstrates that the energy profile of wall-attached motions during the SDS in the logarithmic region of turbulent flows has not yet been explicitly quantified.

2. Methodology and experiment

The coherence statistic in signal processing is a tool for analysing the relationship between two signals. It is frequently employed to calculate the power transfer between the input and output of a linear system. If the signals are ergodic and the system function is linear, the causality between the input and output can be estimated using coherence. The coherence between two signals $x(t)$ and $y(t)$ is defined as

$$\gamma_L^2(f) \equiv \frac{|\langle \tilde{X}(f)\tilde{Y}^*(f)\rangle|^2}{\langle|\tilde{X}(f)|^2\rangle\langle|\tilde{Y}(f)|^2\rangle} = \frac{|\phi_{xy}^{'}(f)|^2}{\phi_{xx}(f)\phi_{yy}(f)}. \tag{2.1}$$

Here, $\tilde{X}(f) = \mathcal{F}[x(t)]$ represents the Fourier transform of signal x in time, and x can be replaced by y. The asterisk $*$ indicates the complex conjugate, $\langle\rangle$ denotes ensemble averaging, and $||$ designates the modulus. Specifically, $0 \le \gamma_L^2 \le 1$ is defined using the linear coherence spectrum (LCS), where γ_L^2 is a function of the frequency f; $\phi_{xy}^{'}$ is the cross-spectrum; ϕ_{xx} and ϕ_{yy} are the autospectral densities of signals x and y, respectively. A similar analysis between different signals using LCS can be found in Baars *et al.* (2016). Consider a linear system with an impulse response $h_l(t)$ defined as $y(t) = h_l(t)x(t)$. In the Fourier domain, this equation becomes $\tilde{Y}(f) = H_L(f)\tilde{X}(f)$, where $H_L(f)$ is the complex-valued linear system transfer function, generally known as spectral linear stochastic estimation (LSE) (also introduced in Adrian (1979), Ewing & Citriniti (1999), Tinney *et al.* (2006) and Baars *et al.* (2016)). Hence, for a linear system,

$$H_L(f) = \frac{\phi_{xy}^{'}(f)}{\phi_{xx}(f)}. \tag{2.2}$$

The system's gain is intuitively connected to the LCS, scaled by the ratio of input-to-output energies, and can be expressed as follows (Bendat & Piersol 2000):

$$|H_L^2(f)| = \gamma_L^2(f)\frac{\phi_{yy}(f)}{\phi_{xx}(f)}. \tag{2.3}$$

A self-similar hierarchy of wall-attached structures inside the logarithmic zone of a TBL (Baidya *et al.* 2019; Deshpande, Monty & Marusic 2019; Marusic & Monty 2019; Hu, Yang & Zheng 2020; Li *et al.* 2022*a*) is idealized in figure 1(*a*). Here, we investigate three hierarchy levels of zones of coherent velocity fluctuations that are randomly positioned, with each hierarchy being represented by a distinct hue. For the sake of simplicity, we define each level's eddy effect volume as having a $l_x \sim \lambda_x$ and $l_z \sim z$ in the x and z directions, respectively, resulting in the aspect ratio of the streamwise/wall-normal direction as $AR = \lambda_x/\Delta z$. To obtain the coherence between two turbulent signals, the position of z_R should be close enough to the wall. In ASL, z_R was selected at the lowest height and the travel signal z_T is the upper position located in the logarithmic regions of TBL as indicated in figure 1(*a*) by z_R and z_T to obtain the coherence.

Baars *et al.* (2017) applied the coherence spectrum to streamwise fluctuating velocity signals at a wall-normal position z_R and a travel signal in the logarithmic region z_T to explore the wall-attached features of turbulent flow. Similar investigations can be found in Krug *et al.* (2019), Baars & Marusic (2020*b*), Duan *et al.* (2020) and Li *et al.* (2022*a*). They imply that, as a consequence of the AEH, the coherence magnitude within the self-similar region adheres to

$$\gamma_L^2 = C_1 \ln\left(\frac{\lambda_x}{\Delta z}\right) + C_2. \tag{2.4}$$

Here, C_1 and C_2 are fit constants, with $C_1 = 0.302$ being a fixed value, and C_2 being affected by the stability/roughness/dust conditions. The statistical aspect ratio (in this case streamwise/wall-normal) then follows:

$$AR = \left.\frac{\lambda_x}{\Delta z}\right|_{\gamma_L^2=0} = \exp\left(\frac{-C_2}{C_1}\right). \tag{2.5}$$

In neutral turbulent flow at $Re_\tau \approx 14\,000$ (laboratory data (Baars *et al.* 2017)), $Re_\tau \approx 2000$ (numerical data, Sillero, Jiménez & Moser 2013) and $Re_\tau \approx 1.4 \times 10^6$ (ASL data, Marusic & Heuer 2007), Baars *et al.* (2017) gave $C_2 = -0.796$ which results in $AR \approx 14$. In addition, Krug *et al.* (2019) found that the self-similar scaling applies also to fluctuations of the spanwise velocity v and the static temperature θ, which will be further extended to PM_{10} in the current work.

Using findings from typical tower micrometeorological data, Davenport (1961) established a trend in the wall-normal coherence of streamwise velocity fluctuation u. The study revealed that turbulent quantities were less coherent as both the vertical separation (Δz) and the wavelength ($\lambda_x = U/f$, where U is the local mean velocity, $f = 50$ Hz is the sampling frequency) decreased. Based on this assumption, the coherence should primarily be affected by the ratio of Δz to λ_x for a certain stability. Davenport (1961) further provided the following empirical formula, noting that the decline in coherence with rising $\Delta z/\lambda_x$ mimics an exponential decay:

$$\gamma_L^2 = \exp\left(-2a\frac{\Delta z}{\lambda_x}\right), \tag{2.6}$$

where a is a decay parameter. For the vertical coherence γ_L^2 of the u component under neutral conditions, Davenport (1961) first stated $a = 7.7$ with regard to the fitting constant

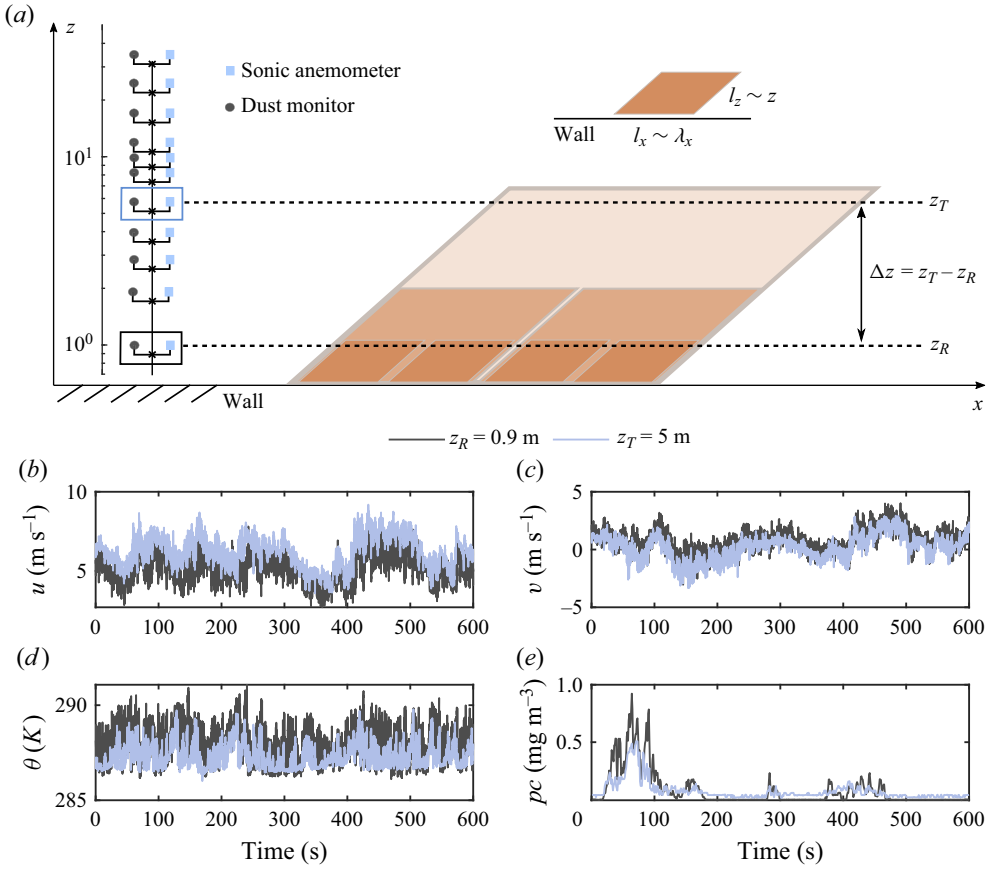

Figure 1. (*a*) The schematic shows isometric *x*–*z* plane views of a hierarchy of self-similar wall-attached eddies representing the logarithmic region, presented as simplified parallelograms (not scaled). Three hierarchical levels are considered, each represented by different colours. Vertical arrays are installed with 11 sonic anemometers (squares) and 11 dust monitors (circles) ranging from 0.9 m to 30 m. The heights, referred to as z_R and z_T, respectively, are set as the fixed near-wall location at $z = 0.9$ m and the travelled heights. Here, $l_x \sim \lambda_x$ and $l_z \sim z$ denote the streamwise and wall-normal extents of the hierarchical level, respectively, with $AR = \lambda_x/\Delta z$ indicating the aspect ratio in the streamwise wall-normal plane. Panels (*b*–*e*) indicate the example signals obtained at $z_R = 0.9$ m and $z_T = 5$ m for the velocity of streamwise component u, the spanwise component v, the temperature θ and the PM_{10} concentration pc, respectively.

in (2.6). Subsequent literature (Pielke & Panofsky 1970; Davison 1976; Berman & Stearns 1977) have reported somewhat revised results and expansions of the concept to spanwise velocity components (v) and the temperature field (θ). It is well acknowledged that a changes with surface-layer stability, being small in intense convection and large in neutral or stable air. Krug *et al.* (2019) provided a depiction of (2.6) with $a = 23$ (e.g. Naito & Kondo 1974), which was observed to closely agree with (2.4) and the data under neutral conditions.

The field measurements of the ASL were taken at the Qingtu Lake Observation Array (QLOA) site in western China during the SDS, and detailed information about the field and data collection can be found in Li *et al.* (2021*a*). The QLOA is located between two of the largest deserts in China: the Badain Jaran Desert and the Tengger Desert, lying within a dusty belt in the Hexi Corridor. Dust weather in the Hexi Corridor is often caused by intense frontal systems, and the flow

No.	Date and time	Duration	Sampling frequency	u_τ (m s^{-1})	z/L	$\bar{U}$ (m s^{-1})	$\overline{pc}$ (mg m^{-3})
D1	28 March 2016, 12:00	2 h	50 Hz	0.33	−0.12	5.74	0.45
D2	28 March 2016, 13:30	2 h	50 Hz	0.35	−0.11	6.13	0.73

Table 1. The key information relating to the datasets during the SDS. Here $\bar{U}$ and $\overline{pc}$ were obtained at $z =$ 0.9 m, indicating the mean velocity and mean PM_{10} concentration. A detailed description of SDS can be seen in Li *et al.* (2021*a*). Note that the sampling frequency for PM_{10} is $f = 1$ Hz.

field and dust field were measured by the current observation site. The data used in this work included wall-normal arrays of sonic anemometers, which performed synchronous measurements of the three-dimensional turbulent flow field. Campbell CSAT3B instruments installed at heights from z_1 to z_{11} were spaced logarithmically from $z = 0.9$ to 30 m ($z = 0.9$, 1.71, 2.5, 3.49, 5, 7.15, 8.5, 10.24, 14.65, 20.96, 30 m) and were employed to acquire time series data of the three components of velocity, as well as the air temperature, at a sampling frequency of 50 Hz. Additionally, dust monitors were installed at corresponding heights to measure the PM_{10} concentration with a frequency of 1 Hz, as illustrated in figure 1(*a*). Figure 1(*b–e*) show an example of data obtained from the ASL to illustrate the streamwise velocity component u, spanwise velocity component v, temperature θ and PM_{10} concentration pc at $z_R = 0.9$ m and $z_T = 5$ m. Throughout this study, we only employ the fluctuating components of the turbulence quantities; the streamwise (or longitudinal), spanwise and wall-normal velocity fluctuations are denoted by u, v and w, respectively, with associated coordinates x, y and z. Temperature fluctuations are denoted by θ, and PM_{10} concentrations are denoted by pc.

Table 1 provides the details of key information for two selected SDS data, where $u_\tau = (-\overline{uw})^{1/2}$ is used to determine the friction velocity at $z = 2.5$ m. The duration extends to 2 h, in comparison with previous ASL literature (e.g. Hutchins *et al.* 2012; Wang & Zheng 2016; Krug *et al.* 2019; Li *et al.* 2022*a*), to ensure a larger number of ensemble runs while performing spectrum analysis on PM_{10} due to the relatively low sampling frequency. The thermal stability of the ASL is generally characterized by the Monin–Obukhov stability parameter z/L (Obukhov 1946; Monin & Obukhov 1954), where $L = -u_\tau^3\bar{\theta}/(\kappa g\overline{w\theta})$ is the Obukhov length, $\kappa = 0.41$ the von Kármán constant, g the gravitational acceleration, $\overline{w\theta}$ the surface heat flux with w and θ the fluctuating wall-normal velocity and temperature components, $\bar{\theta}$ the mean temperature and $z = 2.5$ m is the reference height for evaluating this parameter. In this work, two durations of the dataset were selected to obtain the features of vertical coherence. For the lack of direct measurement of the surface-layer thickness, we assume an estimate for $\delta = 60$ m, following Hutchins *et al.* (2012). Prior to further analysis, the data are adjusted for wind direction and a detrending process is used (see Hutchins *et al.* (2012), Wang & Zheng (2016), for details). While detrending is required to eliminate slow temporal patterns in the data, it also affects coherence at extremely long scales, which must be considered when investigating the data. Thus, raw data were used to apply for coherence, but the detrending process ensures the exploration of the scaling of the logarithmic energy profile for wall-attached eddies.

The spatiotemporal transformation uses Taylor's hypothesis (Taylor 1938), where the local mean velocity is taken as the convection velocity. Taylor's idea is frequently contested in the literature; however, applying it to the current coherence spectrum research should be successful and may not significantly impact the key findings. The findings of Baars

et al. (2017) support this claim, as they demonstrate that both temporal and spatial data produce comparable coherence spectra, except for the near-wall area where the predicted convection velocity is no longer valid (Del Álamo & Jiménez 2009). Since the primary focus of the current investigation is the outer region, the near-wall inaccuracy associated with the application of Taylor's theory is not considered significant in this context.

3. Results

3.1. *Scaling of vertical coherence*

Previous studies (Krug *et al.* 2019; Li *et al.* 2022*a*,*b*) have examined the aspect ratio of AR in u, v and θ under stratified and rough-wall ASL. However, a lack of self-similarity investigation on PM_{10} and u, v and θ under dust-carrying flows will be explored in this work. Figure 2 shows the coherence spectrum γ_L^2 for the two velocity components, the temperature, and PM_{10} concentration in the unstable case with $z/L = -0.12$. It should be noted that, in this case, we choose normalization with Δz since it offers a larger scaling zone. Plotting the findings as shown in figure 2(*a–c*) examines the self-similarity feature as, in this situation, a collapse of curves at various Δz is anticipated, which is also evident in previous ASL results by Krug *et al.* (2019) and Li *et al.* (2022*a*,*b*). We can fit the formula (2.4) to the data and extract the statistical aspect ratio by locating the scaling region by the area of this collapse (highlighted in red in figure 2). For the coherent spectrum of the *pc* in figure 2(*d*), we take the dashed grey line to fit the spectrum based on (2.6) since the lower sampling frequency of the *pc* can not ensure to obtain the smaller scales of structures. The fit in figure 2(*d*) matches well with the raw coherent spectrum at $z_T = 5$ m, further used to fit the other γ_L^2 of the *pc*. Figure 2(*e*) gives a gradual feature of decay on coherence. Generally, the fitting to the lower heights ($\Delta z \lesssim 15$ m) can also be considered that the transportation of PM_{10} indicates wall-attached features with similarity. And the aspect ratio of *pc* is significantly larger than the value of $AR_u \approx 6.2$.

These results are also concluded in table 2, which is also compared with the previous ASL work by Krug *et al.* (2019) and Li *et al.* (2022*a*) at the corresponding stability conditions. Evidently, the results in datasets D1 and D2 are significantly larger than the value of AR obtained under unstable conditions from Li *et al.* (2022*a*) but without the influence of dust. In this study, we conducted the first investigation on the self-similarity of *pm* and further explored the aspect ratio of *pc*. We observed that the value of AR differs between Li *et al.* (2022*a*) and Krug *et al.* (2019), despite both papers describing the self-similarity under a stratified ASL. Since they share the same field observation site, it demonstrates that sand and dust movement dramatically increases the aspect ratio of coherent structures in the flow. It is worth noting that dust monitors continuously measure particle concentration, and data can only be collected when SDS pass through the measurement site. Additionally, we first present the aspect ratio of the PM_{10}, which depicts the similarity features of the dust field.

Previous studies (Wang *et al.* 2020; Liu, Feng & Zheng 2022) suggest that the statistics of turbulent flow undergo changes in sand- or particle-laden two-phase flow. Wang *et al.* (2020) reveal that the inclination angles of large-scale structures tend to increase with sand concentration in atmospheric flow. Moreover, Liu *et al.* (2022) discuss the impacts of particle near-wall movements on turbulence statistics in wind tunnel experiments. Both studies imply that the length scales of turbulent coherent structures are somewhat reduced in sand-laden flows. Consequently, the aspect ratio of u, v and θ is bound to exhibit certain differences. One possible reason is that particulate matters follow the flow field, relying on turbulent motions. Simultaneously, the flow field structures are affected to

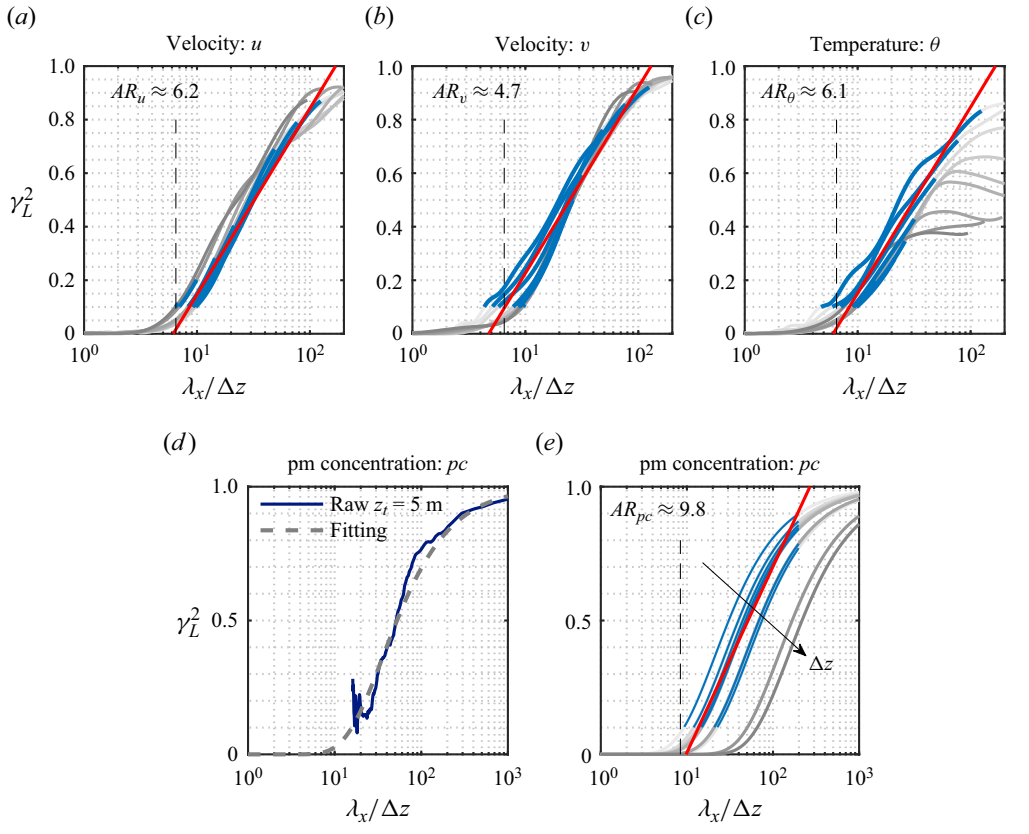

Figure 2. Here γ_L^2 is shown in the range 1.6 m $\leq \Delta z \leq$ 29.1 m (with decreasing Δz indicated by lighter shades of grey) for the following variables: (*a*) streamwise component u; (*b*) spanwise component v; (*c*) temperature θ; (*e*) PM_{10} concentration pc, respectively, in the unstable case with $z/L = -0.11$ (D1). In (*d*), an example of the coherence spectrum γ_L^2 for PM_{10} concentration pc at $z_T = 5$ m is represented by the solid line, and a fitting line with (2.6) is depicted by the dashed line. The red line is a fit according to (2.4) with $C_1 = 0.302$ fixed; the fitting region used is bounded by $\gamma_L^2 > 0.1$ and $\lambda_x < 200$ m and is indicated in blue lines.

	$z/L = -0.12$			$z/L = -0.11$		
	D1	Li *et al.* (2022*a*)	Krug *et al.* (2019)	D2	Li *et al.* (2022*a*)	Krug *et al.* (2019)
AR_u	6.5	4.7	5.9	6.2	4.7	6.0
AR_v	4.9	3.9	4.8	4.7	4.0	4.9
AR_θ	5.8	4.0	5.7	6.1	4.0	5.8
AR_{pc}	8.4	—	—	9.8	—	—

Table 2. The values of AR for u, v, θ and pc are provided at two stability parameters, $z/L = -0.12$ and $z = -0.11$, for datasets D1 and D2. These corresponding values under the stability conditions are also obtained by fitting $AR = a_1 \log(z/L) + a_2$, where a_1 and a_2 are parameters for the velocity and temperature components, as described in Li *et al.* (2022*a*) and Krug *et al.* (2019).

varying degrees in the streamwise and spanwise directions, resulting in an overall increase in AR.

In order to obtain the vertical coherence between two wall-normal signals, an empirically derived transfer kernel comprises implicit filtering to capture the coherent

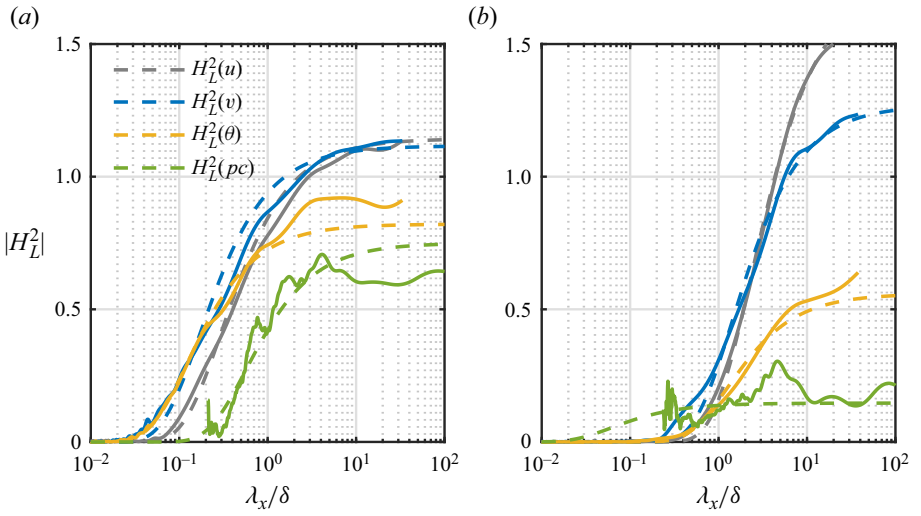

Figure 3. The linear gain $|H_L^2(f)|$ is presented for the z_R and z_T signals of u, v, θ and pc, respectively, in (*a*) $\Delta z/\delta = (z_2 - z_1)/\delta$ and (*b*) $\Delta z/\delta = (z_5 - z_1)/\delta$ by solid coloured lines. The corresponding dashed lines represent fitting lines for $|H_L^2(f)|$ as per (3.1*a*). The stability parameter is $z/L = -0.11$ (D2).

portion in the prediction. Taking the idea from Davenport (1961) to capture the transfer kernel $|H_L^2(f)|$ between the signals in the near-wall and logarithmic regions, the empirical expression follows:

$$|H_L^2(f)| = \exp\left(c_{1i} - \frac{c_{2i}}{\lambda_x/\delta}\right); \quad (i = u, v, \theta \text{ and } pc), \tag{3.1a}$$

$$c_{1i} = A_i \log(\Delta z/\delta) + B_i; \quad c_{2i} = C_i \log(\Delta z/\delta) + D_i. \tag{3.1b}$$

Here, c_{1i} is the extreme parameter, depicting the asymptote value to $\exp(c_1)$ while $\lambda_x/\delta \to \infty$. c_{2i} is a decay parameter, where $i = u, v, \theta$ and pc. Meanwhile, the normalized parameters c_{1i} and c_{2i} are functions of $\Delta z/\delta$, constrained by A_i, B_i, C_i and D_i.

Figure 3 shows the linear gain $|H_L^2(f)|$ as a function of λ_x/δ for u, v, θ and pc at (figure 3*a*) $\Delta z/\delta = (z_2 - z_1)/\delta = (1.71 - 0.9)/60$ and (figure 3*b*) $\Delta z/\delta = (z_5 - z_1)/\delta = (5 - 0.9)/60$. The solid-coloured lines represent the linear gain obtained from (2.3), and the corresponding dashed-coloured lines are fitted by (3.1*a*). As can be seen from the figure, significant matches are indeed observed for all quantities plotted. At lower wavelengths, the kernel of linear gain $|H_L^2(f)|$ reaches zero, indicating that there is no coherence in this region with no coherent energy between inner and outer signals. For the larger wavelengths, the formula (3.1*a*) depicts the trend to asymptote determined by parameter c_1. Notably, the fitting to pc shows the extending estimation at lower wavelengths due to the lower sampling frequency. It should be noted that the linear gain $|H_L^2(f)|$ varies across u, v, θ and pc due to their distinct coherence levels, intuitively linked to the LCS (2.3), caused by variations in AR. In the case of pc, the gain is biased towards larger wavelengths, with a lower maximum gain value compared with the other three components due to weaker coherence of corresponding scales, which is evident from the larger value of AR. Since the linear gain $|H_L^2(f)|$ of pc and θ are smaller than u and v, it can be inferred that the dust and temperature do not follow the flow as closely. As Δz increases, the $|H_L^2(f)|$ of θ and pc decrease significantly, demonstrating that the followability of these two parameters in the normal direction is weaker, particularly for pc.

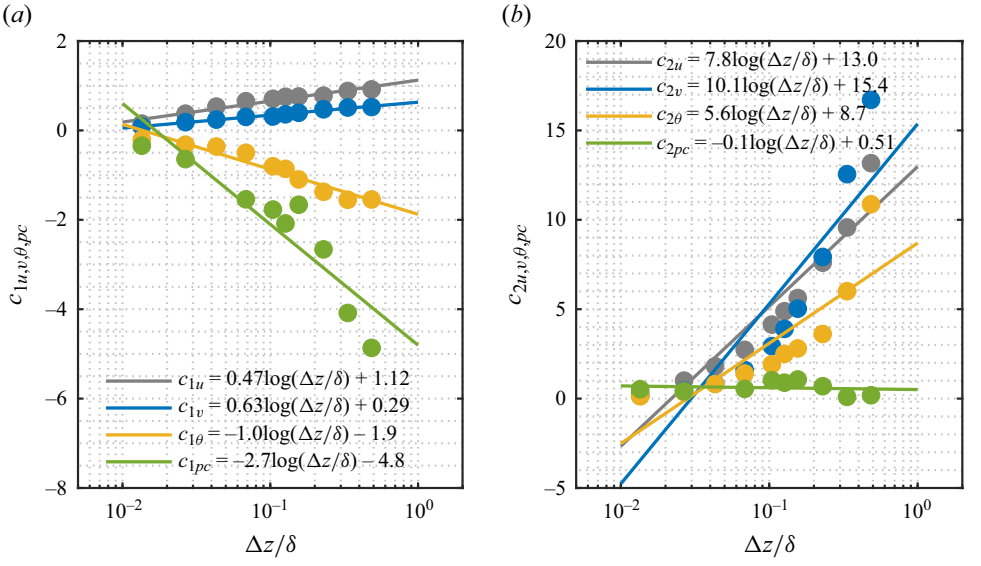

Figure 4. The parameters c_1 in (a) and c_2 in (b) for u, v, θ, and pc vary with $\Delta z/\delta$ according to (3.1a). The solid fitting lines are based on (3.1b). The stability parameter is $z/L = -0.11$ (D2).

	$z/L = -0.12$				$z/L = -0.11$			
	A_i	B_i	C_i	D_i	A_i	B_i	C_i	D_i
u	0.23	0.70	5.30	9.10	0.47	1.12	7.80	13.00
v	0.15	0.42	6.30	10.10	0.63	0.29	10.10	15.40
θ	−0.92	−1.79	8.90	13.30	−1.00	−1.90	5.60	8.70
pc	−2.80	−5.10	−0.23	−0.04	−2.70	−4.80	−0.10	0.51

Table 3. The values of A, B, C and D for u, v, θ and pc in (3.1b) are provided at $z/L = -0.12$ and $z/L = -0.11$.

Once the c_1 and c_2 values are obtained at a certain wall-normal offset Δz, the parameters for A, B, C and D in (3.1b) are easily determined. Figure 4 shows the parameters $c1$ and $c2$ as a function of $\Delta z/\delta$. An empirical parametric equation is fitted to the log–linear trend of SDS data to model the variation. Considering the influence of the current flow from dust-flow interaction and buoyancy-driven effects, the parameters are expected to be explored for the pure shear flow or stratified flow, and even the effects of the Reynolds number could be considered in the future.

In summary of the parameters in (3.1b), table 3 gives a comparison of A, B, C and D at $z/L = -0.12$ and $z/L = -0.11$. Generally, the variation of c_1 and c_2 shows the same trends in both datasets. Meanwhile, the parameters c_1 of the velocity components u and v share the same increasing trend, contrary to the temperature θ and pc. Additionally, the parameters are expected to be compared under neutral conditions to reveal the influence of dust and buoyancy on the features of input–output interactions of the flow.

To exhibit the kernel of linear gain $|H_L^2(f)|$ on different wavelengths λ_x/δ and wall-normal offsets $\Delta z/\delta$, figure 5 indicates the contour plot of $|H_L^2(f)|$ for (figure 5a) u, (figure 5b) v, (figure 5c) θ and (figure 5d) pc, respectively. The red dashed lines

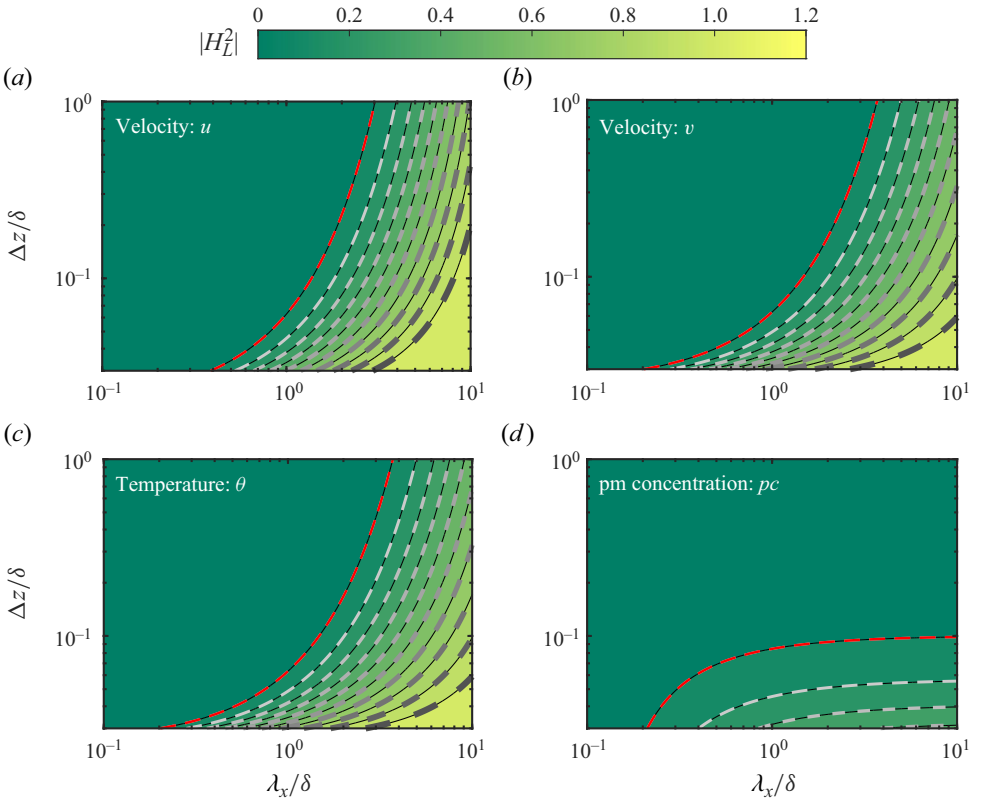

Figure 5. Contour plots of $|H_L^2(f)|$ based on (3.1*a*), (3.1*b*) are shown for (*a*) u, (*b*) v, (*c*) θ and (*d*) pc, respectively, with decreasing values represented by lighter shades of dashed grey lines. The parameters are provided in table 3 at $z/L = -0.12$ (D1). Contour line levels range from 0.1 to 1 with an increment of 0.1, and the red lines correspond to $|H_L^2(f)| = 0.1$.

correspond to $|H_L^2(f)| = 0.1$, and the decreasing values are represented by lighter shades of dashed grey lines. As can be seen, larger wavelengths and lower wall-normal offsets present higher values of $|H_L^2(f)|$ for all components. Generally, the velocity components u, v and temperature θ show great similarity in the variation trend with respect to λ_x/δ and $\Delta z/\delta$. The magnitude of $|H_L^2(f)|$ for pc is much lower than for other components, which may reflect that the ability of dust to follow the flow field determines the energy transfer in input–output signals.

3.2. *Scaling of logarithmic energy profile for wall-attached eddies*

The coherence of a linear system, γ_L^2, therefore represents the fractional part of the output signal power that is produced by the input at that frequency. We can also view the quantity $(1 - \gamma_L^2)$ as an estimate of the fractional power of the output that is not contributed by the input at a particular frequency. This naturally leads to the definition of the coherent/incoherent output spectrum,

$$\phi_{uu}(z_T; \lambda_x) = \underbrace{(\gamma_L^2)\phi_{uu}(z_T; \lambda_x)}_{coherent} + \underbrace{(1 - \gamma_L^2)\phi_{uu}(z_T; \lambda_x)}_{incoherent}, \tag{3.2a}$$

$$\overline{u^2}^+(z_T)|_{coherent} = \int_0^\infty (\gamma_L^2)\phi_{uu}(z_T;\lambda_x)\,\mathrm{d}\lambda_x, \tag{3.2b}$$

$$\overline{u^2}^+(z_T)|_{incoherent} = \int_0^\infty (1-\gamma_L^2)\phi_{uu}(z_T;\lambda_x)\,\mathrm{d}\lambda_x. \tag{3.2c}$$

Here, $\overline{u^2}^+(z_T)|_{coherent}$ corresponds to the energy of motions attached to the wall; otherwise, $\overline{u^2}^+(z_T)|_{incoherent}$ reflects the detached portion. Following the separation of the coherent and incoherent portions of the streamwise turbulence intensities, the LCS can be used as a wavelength-dependent filter for decomposing ϕ_{uu} into stochastically coherent and incoherent portions relative to the signal $u(t, z_R)$, as demonstrated in the previous work by Baars & Marusic (2020*a*).

The input signal is convolved with a first-order transfer kernel, $H_L(f)$, to create the output. Only the linear mechanism of energy transfer is accounted for by the convolution, as the output is proportionate to the input. The analysis permits nonlinear energy transfer when higher-order terms in (3.3*a*) and (3.3*b*) are retained. Higher-order estimating approaches have been the focus of several investigations in wall-bounded turbulence. One noteworthy example is the formulation by Naguib, Wark & Juckenhöfel (2001) of a time-domain quadratic scheme that included estimates of the velocity field in a TBL given surface pressures as an input; their stochastic estimates improved upon the addition of the quadratic elements. Additionally, the reader is directed to the works mentioned above as well as the discussion in Baars & Tinney (2014) for information on the specifics of higher-order approaches. The extraordinary concordance between LSE and conditionally averaged fields in TBL flow, which has applicability to the current ASL flow, was highlighted in Adrian, Moin & Moser (1987) and Baars *et al.* (2016).

While the transfer gain embeds the scaling of each Fourier component in the estimate, the shift of each Fourier mode is embedded in the phase, which yields the LSE in (3.3*a*). For LSE, we use a combination of the filtered gain factor and the original phase to form a new kernel in (3.3*a*). Although an inconsistent phase exists at the smaller wavelengths, it will not impact the estimation due to the zero-valued gain factor at these incoherent wavelengths. Finally, the time-domain conditional estimate is obtained by the inverse Fourier transform for both 'with phase' and 'without phase' in the form of (3.3*a*) and (3.3*b*). Meanwhile, the Fourier spectrum of the predicted signal $y_{LSE}(t)$ by LSE can be written as (3.3*c*), further the turbulent intensity for $y_{LSE}(t)$ acquired in (3.3*d*):

$$y_{LSE}(t) = \mathcal{F}^{-1}(H_L\mathcal{F}[x(t)]) \quad \text{(with phase)}, \tag{3.3a}$$

$$y_{LSE}(t) = \mathcal{F}^{-1}(|H_L|\mathcal{F}[x(t)]) \quad \text{(without phase)}, \tag{3.3b}$$

$$\phi_{uu}(z_T;\lambda_x)|_{LSE} = |\mathcal{F}[y_{LSE}(t)]|^2, \tag{3.3c}$$

$$\overline{u^2}^+(z_T)|_{LSE} = \int_0^\infty \phi_{uu}(z_T;\lambda_x)|_{LSE}\,\mathrm{d}\lambda_x. \tag{3.3d}$$

By connecting to (3.2*b*), a stochastic estimate of the output's energy spectrum can be expressed as (3.3*d*), which yields to

$$\phi_{uu}(z_T;\lambda_x)|_{LSE} = |H_L^2(f)|\phi_{uu}(z_R;\lambda_x) = \gamma_L^2\phi_{uu}(z_T;\lambda_x). \tag{3.4}$$

It is the equivalent form of (2.3). This implies that the amount of energy of z_T that can be reconstructed via an LSE procedure, from input z_R, is equal to the measured spectrum at z_T, multiplied by γ_L^2, which is also applied to the TBL in Baars *et al.* (2017) and Baars &

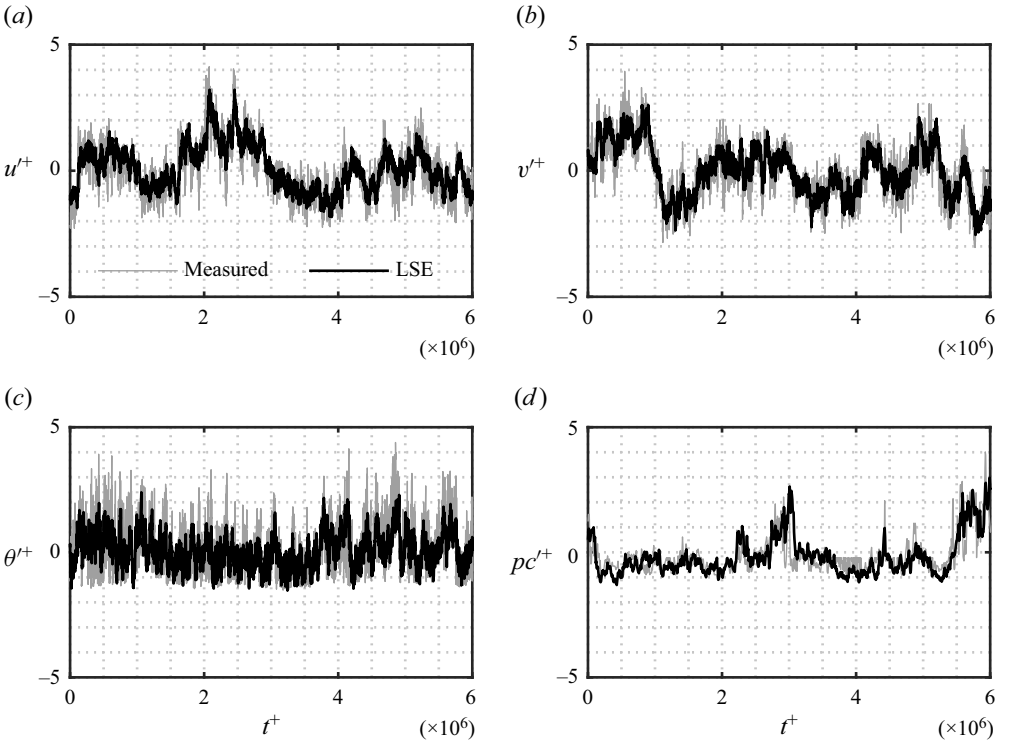

Figure 6. The figure displays time series data at $z/L = -0.12$ (D1), with the measured signals represented in grey and the corresponding constructed output signals shown in black. The construction employs a first-order transfer kernel, as defined by (3.3*b*). The values of u'^+, v'^+, θ'^+ and pc'^+ are normalized by their respective standard deviations.

Marusic (2020*a*). It should be noted that (3.4) includes not only wall-attached self-similar motions but also wall coherent motions scaled by the outer scale (i.e. wall-attached non-self-similar motion) which is discussed in the previous works (Baars & Marusic 2020*a*; Deshpande *et al.* 2020; Hwang, Lee & Sung 2020). Moreover, Davenport (1961) implies the possibility of self-similar motions among wall-incoherent motions (Krug *et al.* 2019). The detached self-similar structures in several studies (Marusic & Monty 2019; Yoon *et al.* 2020) have also been discussed.

Figure 6 shows the fluctuations of the measured signals in grey and the constructed output signals by (3.3*b*) in black. The gain function in figure 3 and (2.2) can be interpreted as an experimentally calculated scale filter because it shows a steady roll-off. As suggested by Baars *et al.* (2016), the LSE eliminates the need for an *a priori* choice of a separation scale, which is necessary for large-wavelength pass-filtering of the input and output signals. Scaling the transfer kernel gain allows for the prediction of a filter that retains only the coherent scales of the acquired input.

Based on the empirical fitting in (3.1*a*) and (3.3*b*), a premultiplied energy spectrum of the conditional estimate is shown in figure 7, alongside the raw output spectra and estimated spectrum by LSE procedure. In figure 7, arbitrary input–output pairs of dataset $z_R = 0.9$ m to $z_T = 5$ m for u, v, w and pc, are chosen to illustrate the LSE of the premultiplied spectrum, where the process is called LSE-based in the current study. The smaller wavenumber (corresponding to larger scales) of the spectrum is indicated in

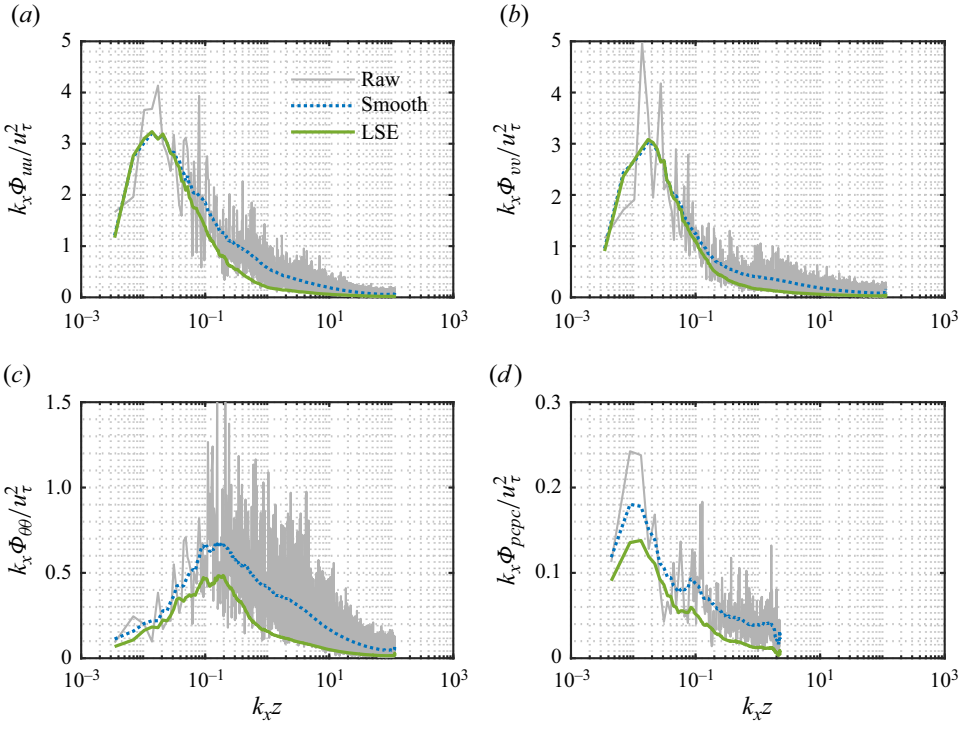

Figure 7. Premultiplied energy spectra of the output signal at $z_T = 5$ m, with the raw signal depicted in grey and the corresponding smoothed signal shown in blue at $z/L = -0.12$ (D1). The signals are decomposed into coherent contributions represented in green, relative to (3.2*a*). Panels (*a–d*) correspond to u, v, θ and pc, respectively.

figure 7. In other words, the linearly estimated spectrum constitutes less energy due to the lack of perfect coherence (the visual implication of (2.2)).

Townsend (1976) and Perry & Chong (1982) established the theory that the interior part of the inertial region requires a logarithmic profile for the streamwise turbulence intensities, giving a Townsend–Perry constant $A_1 = 1.26$ to depict the slope of the logarithmic profile, which has been supported by Marusic *et al.* (2013). According to Townsend's AEH, the wall-normal logarithmic decay of turbulence intensity can be extended to the logarithmic decay of wall-attached turbulence intensity. More recently, Li *et al.* (2021*b*) also support the logarithmic decay of turbulence intensity for wall-attached eddies in the spanwise direction. For the LSE-based turbulence intensities for u, v, θ and pc, we postulate that coherent and incoherent portions also feature a logarithmic energy distribution as follows:

$$\overline{u^2}^+(\Delta z) = B_1 - A_1 \ln(\Delta z/\delta), \tag{3.5a}$$

$$\overline{u^2}^+(\Delta z)|_{coh} = P_c - Q_c \ln(\Delta z/\delta), \tag{3.5b}$$

$$\overline{u^2}^+(\Delta z)|_{incoh} = P_i - Q_i \ln(\Delta z/\delta), \tag{3.5c}$$

where $A_1 = 1.26$ represents the Townsend–Perry constant under neutral conditions for the streamwise velocity component, and Q_c and P_c denote the fitting parameters governing the self-similar logarithmic behaviour of LSE-based turbulence intensities (corresponding

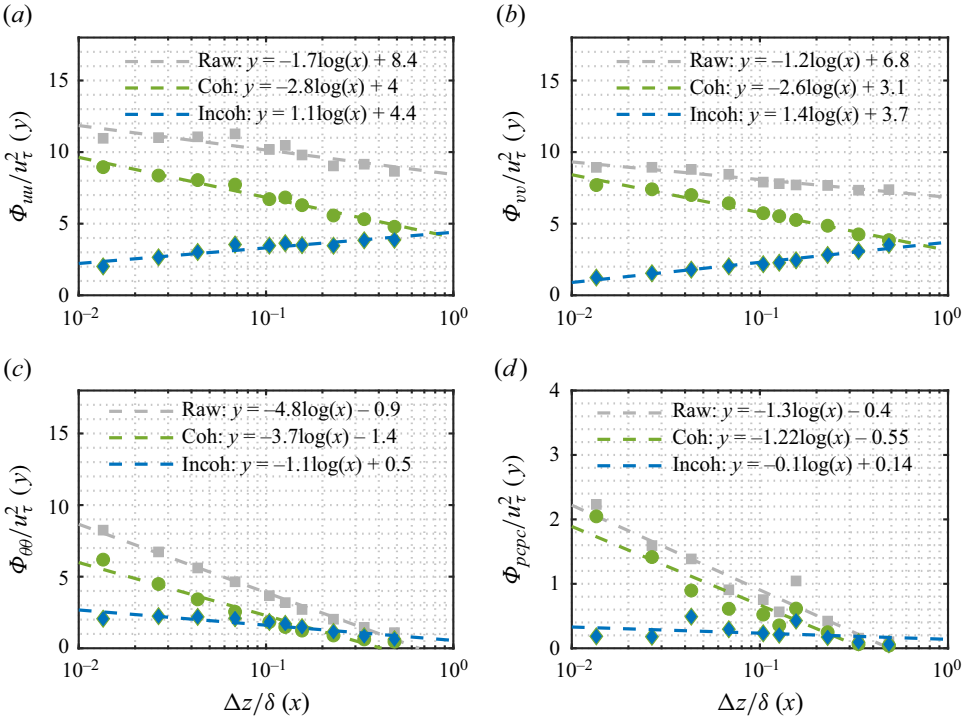

Figure 8. Turbulence intensity profiles along the wall-normal offset, with the raw, coherent (Coh) and incoherent (Incoh) depicted in grey, green and blue, respectively, at $z/L = -0.12$ (D1). The dashed lines represent fitting lines based on (3.5*a*), (3.5*b*) and (3.5*c*), respectively. Panels (*a–d*) correspond to u, v, θ and *pc*, respectively.

to the coherent portions). Here Q_i and P_i are fitting parameters used to characterize the logarithmic behaviour of the incoherent portions.

Significantly, the value assigned to A_1 has undergone significant alterations over time. A key aspect contributing to this discrepancy is that (3.5*a*) is confined to attached-eddy turbulence exclusively, while measures of the total streamwise TKE encompass additional contributions. Thus far, our understanding of turbulent intensity scaling within the logarithmic region, as articulated by the AEH, has been well-established. We firmly believe that the coherent component in the current signal decomposition primarily comprises vortex structures exhibiting self-similarity in scale. Previous investigations by Marusic & Kunkel (2003), Kunkel & Marusic (2006) and Wang & Zheng (2016) have highlighted that turbulent energy, particularly at elevated Reynolds numbers in atmospheric flows, adheres to a logarithmic law. This body of evidence indicates that turbulent energy in flows governed by attached eddies approximately adheres to the principles of the AEH within the logarithmic region.

In our current study, we operate under the assumption that attached eddy structures predominate in $\overline{u^2}$ within atmospheric observations, thereby leading to the logarithmic behaviour observed in the coherent component. Contributions from different eddy types to inner flow-scaled premultiplied u-spectra, with scaling and overlap regions following Perry *et al.* (1986), where these contributions are referred to as Type A, B and C energy contributions (Perry & Marusic 1995; Marusic & Monty 2019). Type-A eddies are attached and self-similar, and only these are part of the AEH. In the context of low wavenumbers.

	$z/L = -0.12$				$z/L = -0.11$				$z/L = 0$ (Neutral)
	u	v	θ	pc	u	v	θ	pc	u
A_1	1.7	1.2	4.8	1.3	1.4	1.7	5.0	2.4	≈1.3 (Marusic *et al.* 2013)
Q_c	2.8	2.6	3.7	1.2	3.1	3.2	4.0	2.2	≈0.98 (Baars & Marusic 2020*b*)
Q_i	−1.1	−1.4	1.1	0.1	−1.7	−1.4	0.9	0.1	

Table 4. The fitting parameters of the slope A_1, Q_c and Q_i for u, v, θ and pc in (3.5*a*), (3.5*b*) and (3.5*c*) are provided for two stability conditions, $z/L = -0.12$ and $z/L = -0.11$, comparing with the neutral conditions by Marusic *et al.* (2013) and Baars & Marusic (2020*b*).

Type-B energy is postulated to originate from detached motions, which encompasses Type-C energy emanating from Kolmogorov scales and small-scale detached eddies. Should we postulate that the behaviour of the incoherent component follows a logarithmic trajectory, it can be expressed as (3.5*c*). Hence, the incoherent component should also adhere to a logarithmic pattern: $P_i = B_1 - P_c$ and $Q_i = A_1 - Q_c$, a proposition supported by the parameters illustrated in figure 8 and table 4. Additionally, analogous findings regarding the logarithmic distribution for both coherent and incoherent components are evident in Li *et al.* (2021*b*). It should be emphasized that the parameters adhere to a relationship based on $A_1 = Q_c + Q_i$.

Figure 8 gives turbulence intensity profiles for u, v, θ and pc along the wall-normal offset $\Delta z/\delta$. The raw signal and LSE-based turbulence intensities are fitted as grey, green and blue lines based on (3.5*a*), qs (3.5*b*) and (3.5*c*), respectively. The log–linear manner is obvious to see for all quantities, being evident as a proper way to depict the scaling law.

The variations in A_1, Q_c and Q_i for u, v, θ and pc based on (3.5*a*) and (3.5*b*) for datasets D1 and D2 are presented in table 4. Obviously, the slope of turbulence intensity for LSE-based Q_c is much bigger than $A1$ for u and v. On the contrary, the slope of θ and pc for A_1 is somewhat larger. We also give a comparison of A_1 and Q_c for u under neutral condition with Marusic *et al.* (2013) and Baars & Marusic (2020*b*) to indicate the difference of parameters obtained during SDS. It is necessary to consider abundant atmospheric features (e.g. buoyancy, roughness, dust emission) while arguing for self-similarity in high Reynolds numbers. Consequently, it would be helpful to understand how the logarithmic decay of turbulence intensity changes under increasing buoyancy conditions. For the current study, the slope of the logarithmic decay of turbulence intensity for wall-attached eddies during SDS is also influenced by a varied Townsend–Perry constant in neutral shear flow, as discussed by Baars & Marusic (2020*b*), with the additional consideration of buoyancy and dust field effects.

4. Conclusion

We have demonstrated the implications of Townsend's AEH for the coherence trend, which is also supported by turbulence during the SDS. The self-similarity assumptions/hypotheses do seem to hold for PM_{10} data at lower heights. The aspect ratio for PM_{10} in the streamwise/wall-normal plane (AR_{pc}) is much larger than the aspect ratio for velocity and temperature components. Following the idea from Davenport (1961), this work derived an empirical transfer kernel $|H_L^2(f)| = \exp(c_1 - c_2\delta/\lambda_x)$ to depict the coherence between the near-wall reference position and the travelled signal in higher heights for u, v, θ and pc. After fitting the transfer kernel as a function of wall-normal offset (Δz) and wavelength (λ_x), the contour features of $|H_L^2(f)|$ for all four components

indicate that larger wavelengths and lower wall-normal offsets present higher values. The eddies are distinguished as coherent and incoherent by the LCS. Upon separating, the energy profile for wall-attached eddies for u, v, θ and pc all obey the log–linear manner, giving a slope larger than the Townsend–Perry constant (≈0.98 from Baars & Marusic (2020*b*)) during the SDS.

The established logarithmic behaviour of second-order statistics proposed by this paper is beneficial for improving existing wall models in numerical simulations. One direct application is to assess the simulated results. Due to the fact there is lack of information for atmospheric boundary layer flow at various Reynolds number, the given logarithmic law for the second-order moments (i.e. $\overline{u^2}^+$,$\overline{\theta^2}^+$, etc) can be utilised to appraise the near wall behaviour of simulated flow, thermal and scalar quantities via either Reynolds-averaged Navier–Stokes or large-eddy simulation (LES) at different Reynolds number. For instance, Stevens, Wilczek & Meneveau (2014) assessed the performance of LES for the generalized logarithmic law of second- and high-order moments via AEH (Marusic *et al.* 2013; Meneveau & Marusic 2013). This serves as an extra guide for the accuracy of numerical simulations, apart from comparing the mean profiles of velocity, temperature and scalar fields. Moreover, in term of the prediction of the small particle dispersion, it is also interesting to incorporate the effect of non-uniform TKE along wall-normal direction (Gorlé *et al.* 2009), such as approximating the inner scaled TKE $\simeq 3/2\overline{u^2}^+$.

As a final note, while the current study is confined to vertical coherence, particularly on the lower sampling frequency of PM_{10} data, expanding the similarity to SDS events strengthens predictions and applicability to wall-attached features.

Acknowledgements. We express our sincere gratitude to X. Xu for providing constructive discussion. The authors also appreciate the valuable comments made by the anonymous referees which helped to improve both the quality and the presentation of this paper.

Funding. We acknowledge support from the Scientific Research Foundation of Chongqing University of Technology (2022ZDZ017) and the Youth Project of Science and Technology Research Program of Chongqing Education Commission of China (KJQN202201141).

Declaration of interests. The authors report no conflict of interest.

Author ORCIDs.
Xuebo Li https://orcid.org/0000-0001-7139-8923;
Lan Hu https://orcid.org/0000-0002-4090-0471;
Wanting Liu https://orcid.org/0000-0001-6204-0436.

References

Adrian, R.J. 1979 Conditional eddies in isotropic turbulence. *Phys. Fluids* **22** (11), 2065–2070.

Adrian, R.J., Moin, P. & Moser, R.D. 1987 Stochastic estimation of conditional eddies in turbulent channel flow. In *Studying Turbulence Using Numerical Simulation Databases. Proceedings of the 1987 Summer Program*. Stanford University.

Akhlaq, M., Sheltami, T.R. & Mouftah, H.T. 2012 A review of techniques and technologies for sand and dust storm detection. *Rev. Environ. Sci. Bio/Technol.* **11**, 305–322.

Albarakat, R. & Lakshmi, V. 2019 Monitoring dust storms in Iraq using satellite data. *Sensors* **19** (17), 3687.

Baars, W.J., Hutchins, N. & Marusic, I. 2016 Spectral stochastic estimation of high-Reynolds-number wall-bounded turbulence for a refined inner-outer interaction model. *Phys. Rev. Fluids* **1** (5), 054406.

Baars, W.J., Hutchins, N. & Marusic, I. 2017 Self-similarity of wall-attached turbulence in boundary layers. *J. Fluid Mech.* **823**, R2.

Baars, W.J. & Marusic, I. 2020*a* Data-driven decomposition of the streamwise turbulence kinetic energy in boundary layers. Part 1. Energy spectra. *J. Fluid Mech.* **882**, A25.

BAARS, W.J. & MARUSIC, I. 2020*b* Data-driven decomposition of the streamwise turbulence kinetic energy in boundary layers. Part 2. Integrated energy and a_1. *J. Fluid Mech.* **882**, A26.

BAARS, W.J. & TINNEY, C.E. 2014 Proper orthogonal decomposition-based spectral higher-order stochastic estimation. *Phys. Fluids* **26** (5), 055112.

BAIDYA, R., *et al.* 2019 Simultaneous skin friction and velocity measurements in high Reynolds number pipe and boundary layer flows. *J. Fluid Mech.* **871**, 377–400.

BAIDYA, R., PHILIP, J., HUTCHINS, N., MONTY, J.P. & MARUSIC, I. 2017 Distance-from-the-wall scaling of turbulent motions in wall-bounded flows. *Phys. Fluids* **29** (2), 020712.

BANTA, R.M., PICHUGINA, Y.L. & BREWER, W.A. 2006 Turbulent velocity-variance profiles in the stable boundary layer generated by a nocturnal low-level jet. *J. Atmos. Sci.* **63** (11), 2700–2719.

BASLEY, J., PERRET, L. & MATHIS, R. 2019 Structure of high Reynolds number boundary layers over cube canopies. *J. Fluid Mech.* **870**, 460–491.

BENDAT, J.S. & PIERSOL, A.G. 2000 Random data analysis and measurement procedures. *Meas. Sci. Technol.* **11** (12), 1825–1826.

BERMAN, S. & STEARNS, C.R. 1977 Near-earth turbulence and coherence measurements at Aberdeen Proving Ground, MD. *Boundary-Layer Meteorol.* **11**, 485–506.

DAVENPORT, A.G. 1961 The spectrum of horizontal gustiness near the ground in high winds. *Q. J. R. Meteorol.* **87** (372), 194–211.

DAVISON, D.S. 1976 Geometric similarity for the temperature field in the unstable atmospheric surface layer. *Boundary-Layer Meteorol.* **10** (2), 167–180.

DEL ÁLAMO, J.C. & JIMÉNEZ, J. 2009 Estimation of turbulent convection velocities and corrections to Taylor's approximation. *J. Fluid Mech.* **640**, 5–26.

DEL ALAMO, J.C., JIMÉNEZ, J., ZANDONADE, P. & MOSER, R.D. 2006 Self-similar vortex clusters in the turbulent logarithmic region. *J. Fluid Mech.* **561**, 329–358.

DESHPANDE, R., CHANDRAN, D., MONTY, J.P. & MARUSIC, I. 2020 Two-dimensional cross-spectrum of the streamwise velocity in turbulent boundary layers. *J. Fluid Mech.* **890**, R2.

DESHPANDE, R., MONTY, J.P. & MARUSIC, I. 2019 Streamwise inclination angle of large wall-attached structures in turbulent boundary layers. *J. Fluid Mech.* **877**, R4.

DRITSELIS, C.D. & VLACHOS, N.S. 2008 Numerical study of educed coherent structures in the near-wall region of a particle-laden channel flow. *Phys. Fluids* **20** (5), 055103.

DRITSELIS, C.D. & VLACHOS, N.S. 2011 Numerical investigation of momentum exchange between particles and coherent structures in low *Re* turbulent channel flow. *Phys. Fluids* **23** (2), 025103.

DUAN, Y., ZHANG, P., ZHONG, Q., ZHU, D. & LI, D. 2020 Characteristics of wall-attached motions in open channel flows. *Phys. Fluids* **32** (5), 055110.

EWING, D. & CITRINITI, J.H. 1999 Examination of a LSE/POD complementary technique using single and multi-time information in the axisymmetric shear layer. In *IUTAM Symposium on Simulation and Identification of Organized Structures in Flows: Proceedings of the IUTAM Symposium held in Lyngby, Denmark, 25–29 May 1997*, pp. 375–384. Springer.

FAVRE, A., GAVIGLIO, J. & DUMAS, R. 1967 Structure of velocity space-time correlations in a boundary layer. *Phys. Fluids* **10** (9), S138–S145.

GANAPATHISUBRAMANI, B., LONGMIRE, E.K. & MARUSIC, I. 2003 Characteristics of vortex packets in turbulent boundary layers. *J. Fluid Mech.* **478**, 35–46.

GORLÉ, C., VAN BEECK, J., RAMBAUD, P. & VAN TENDELOO, G. 2009 CFD modelling of small particle dispersion: the influence of the turbulence kinetic energy in the atmospheric boundary layer. *Atmos. Environ.* **43** (3), 673–681.

HU, R., YANG, X.I.A. & ZHENG, X. 2020 Wall-attached and wall-detached eddies in wall-bounded turbulent flows. *J. Fluid Mech.* **885**, A30.

HULTMARK, M., VALLIKIVI, M., BAILEY, S.C.C. & SMITS, A.J. 2012 Turbulent pipe flow at extreme Reynolds numbers. *Phys. Rev. Lett.* **108** (9), 094501.

HUTCHINS, N., CHAUHAN, K., MARUSIC, I., MONTY, J.P. & KLEWICKI, J. 2012 Towards reconciling the large-scale structure of turbulent boundary layers in the atmosphere and laboratory. *Boundary-Layer Meteorol.* **145** (2), 273–306.

HUTCHINS, N. & MARUSIC, I. 2007 Evidence of very long meandering features in the logarithmic region of turbulent boundary layers. *J. Fluid Mech.* **579**, 1–28.

HWANG, J., LEE, J.H. & SUNG, H.J. 2020 Statistical behaviour of self-similar structures in canonical wall turbulence. *J. Fluid Mech.* **905**, A6.

HWANG, J. & SUNG, H.J. 2018 Wall-attached structures of velocity fluctuations in a turbulent boundary layer. *J. Fluid Mech.* **856**, 958–983.

HWANG, J. & SUNG, H.J. 2019 Wall-attached clusters for the logarithmic velocity law in turbulent pipe flow. *Phys. Fluids* **31** (5), 055109.

HWANG, Y. 2015 Statistical structure of self-sustaining attached eddies in turbulent channel flow. *J. Fluid Mech.* **767**, 254–289.

JIMÉNEZ, J. 2012 Cascades in wall-bounded turbulence. *Annu. Rev. Fluid Mech.* **44**, 27–45.

JIMÉNEZ, J. 2018 Coherent structures in wall-bounded turbulence. *J. Fluid Mech.* **842**, P1.

JIMÉNEZ, J. & HOYAS, S. 2008 Turbulent fluctuations above the buffer layer of wall-bounded flows. *J. Fluid Mech.* **611**, 215–236.

KATUL, G.G., PORPORATO, A. & NIKORA, V. 2012 Existence of k^{-1} power-law scaling in the equilibrium regions of wall-bounded turbulence explained by Heisenberg's eddy viscosity. *Phys. Rev.* E **86**, 066311.

KRUG, D., BAARS, W.J., HUTCHINS, N. & MARUSIC, I. 2019 Vertical coherence of turbulence in the atmospheric surface layer: connecting the hypotheses of Townsend and Davenport. *Boundary-Layer Meteorol.* 1–16.

KUNKEL, G.J. & MARUSIC, I. 2006 Study of the near-wall-turbulent region of the high-Reynolds-number boundary layer using an atmospheric flow. *J. Fluid Mech.* **548**, 375–402.

LEE, M. & MOSER, R.D. 2015 Direct numerical simulation of turbulent channel flow up to $Re_\tau \approx 5200$. *J. Fluid Mech.* **774**, 395–415.

LI, J., WANG, H., LIU, Z., CHEN, S. & ZHENG, C. 2012 An experimental study on turbulence modification in the near-wall boundary layer of a dilute gas-particle channel flow. *Exp. Fluids* **53**, 1385–1403.

LI, X., HUANG, Y., WANG, G. & ZHENG, X. 2021*a* High-frequency observation during sand and dust storms at the Qingtu Lake observatory. *Earth Syst. Sci. Data* **13** (12), 5819–5830.

LI, X., HUTCHINS, N., ZHENG, X., MARUSIC, I. & BAARS, W.J. 2022*a* Scale-dependent inclination angle of turbulent structures in stratified atmospheric surface layers. *J. Fluid Mech.* **942**, A38.

LI, X., WANG, G. & ZHENG, X. 2021*b* Logarithmic energy profile of the streamwise velocity for wall-attached eddies along the spanwise direction in turbulent boundary layer. *Phys. Fluids* **33** (10), 105119.

LI, X., WANG, G. & ZHENG, X. 2022*b* Turbulent/synoptic separation and coherent structures in the atmospheric surface layer for a range of surface roughness. *Boundary-Layer Meteorol.* **182** (1), 75–93.

LIU, H., FENG, Y. & ZHENG, X. 2022 Experimental investigation of the effects of particle near-wall motions on turbulence statistics in particle-laden flows. *J. Fluid Mech.* **943**, A8.

LIU, T., *et al.* 2023 Classification and sources of extremely severe sandstorms mixed with haze pollution in Beijing. *Environ. Pollut.* **322**, 121154.

LOZANO-DURÁN, A., FLORES, O. & JIMÉNEZ, J. 2012 The three-dimensional structure of momentum transfer in turbulent channels. *J. Fluid Mech.* **694**, 100–130.

LOZANO-DURÁN, A. & JIMÉNEZ, J. 2014 Time-resolved evolution of coherent structures in turbulent channels: characterization of eddies and cascades. *J. Fluid Mech.* **759**, 432–471.

MARUSIC, I., BAARS, W.J. & HUTCHINS, N. 2017 Scaling of the streamwise turbulence intensity in the context of inner-outer interactions in wall turbulence. *Phys. Rev. Fluids* **2** (10), 100502.

MARUSIC, I. & HEUER, W.D.C. 2007 Reynolds number invariance of the structure inclination angle in wall turbulence. *Phys. Rev. Lett.* **99** (11), 114504.

MARUSIC, I. & KUNKEL, G.J. 2003 Streamwise turbulence intensity formulation for flat-plate boundary layers. *Phys. Fluids* **15** (8), 2461–2464.

MARUSIC, I., MCKEON, B.J., MONKEWITZ, P.A. & NAGIB, H. 2010 Wall-bounded turbulent flows at high Reynolds numbers: recent advances and key issues. *Phys. Fluids* **22** (6), 65103–65103.

MARUSIC, I. & MONTY, J.P. 2019 Attached eddy model of wall turbulence. *Annu. Rev. Fluid Mech.* **51**, 49–74.

MARUSIC, I., MONTY, J.P., HULTMARK, M. & SMITS, A.J. 2013 On the logarithmic region in wall turbulence. *J. Fluid Mech.* **716**, R3.

MENEVEAU, C. & MARUSIC, I. 2013 Generalized logarithmic law for high-order moments in turbulent boundary layers. *J. Fluid Mech.* **719**, R1.

MIDDLETON, N. & KANG, U. 2017 Sand and dust storms: impact mitigation. *Sustainability* **9** (6), 1053.

MONIN, A. & OBUKHOV, A.M. 1954 Basic laws of turbulent mixing in the surface layer of the atmosphere. *Contrib. Geophys. Inst. Acad. Sci. USSR* **151** (163), e187.

NAGUIB, A.M., WARK, C.E. & JUCKENHÖFEL, O. 2001 Stochastic estimation and flow sources associated with surface pressure events in a turbulent boundary layer. *Phys. Fluids* **13** (9), 2611–2626.

NAITO, G. & KONDO, J. 1974 Spatial structure of fluctuating components of the horizontal wind speed above the ocean. *JMSJ Ser. II* **52** (5), 391–399.

NICKELS, T.B., MARUSIC, I., HAFEZ, S. & CHONG, M.S. 2005 Evidence of the k_1^{-1} law in a high-Reynolds-number turbulent boundary layer. *Phys. Rev. Lett.* **95** (7), 074501.

NIKORA, V. 1999 Origin of the '-1' spectral law in wall-bounded turbulence. *Phys. Rev. Lett.* **83**, 734–736.

OBUKHOV, A.M. 1946 Turbulence in an atmosphere with inhomogeneous temperature, TR. *Inst. Teor. Geofis. Akad. Nauk SSSR* **1**, 95–115.

PERRY, A.E. & ABELL, C.J. 1977 Asymptotic similarity of turbulence structures in smooth- and rough-walled pipes. *J. Fluid Mech.* **79** (04), 785–799.
PERRY, A.E. & CHONG, M.S. 1982 On the mechanism of wall turbulence. *J. Fluid Mech.* **119**, 173–217.
PERRY, A.E., HENBEST, S. & CHONG, M.S. 1986 A theoretical and experimental study of wall turbulence. *J. Fluid Mech.* **165**, 163–199.
PERRY, A.E. & MARUSIC, I. 1995 A wall-wake model for the turbulence structure of boundary layers. Part 1. Extension of the attached eddy hypothesis. *J. Fluid Mech.* **298**, 361–388.
PIELKE, R.A. & PANOFSKY, H.A. 1970 Turbulence characteristics along several towers. *Boundary-Layer Meteorol.* **1**, 115–130.
ROBINSON, S.K. 1991 Coherent motions in the turbulent boundary layer. *Annu. Rev. Fluid Mech.* **23** (1), 601–639.
ROSENBERG, B.J., HULTMARK, M., VALLIKIVI, M., BAILEY, S.C.C. & SMITS, A.J. 2013 Turbulence spectra in smooth- and rough-wall pipe flow at extreme Reynolds numbers. *J. Fluid Mech.* **731**, 46–63.
SALESKY, S.T. & ANDERSON, W. 2020 Coherent structures modulate atmospheric surface layer flux-gradient relationships. *Phys. Rev. Lett.* **125** (12), 124501.
SILLERO, J.A., JIMÉNEZ, J. & MOSER, R.D. 2013 One-point statistics for turbulent wall-bounded flows at Reynolds numbers up to $\delta^+ \approx 2000$. *Phys. Fluids* **25** (10), 105102.
SIVAKUMAR, M.V.K. 2005 Impacts of sand storms/dust storms on agriculture. In *Natural Disasters and Extreme Events in Agriculture: Impacts and Mitigation*, pp. 159–177. Springer.
SONG, L., BI, X., ZHANG, Z., LI, L., DAI, Q., ZHANG, W., LI, H., WANG, X., LIANG, D. & FENG, Y. 2022 Impact of sand and dust storms on the atmospheric environment and its source in Tianjin-China. *Sci. Total Environ.* **825**, 153980.
STEVENS, R.J.A.M., WILCZEK, M. & MENEVEAU, C. 2014 Large-eddy simulation study of the logarithmic law for second- and higher-order moments in turbulent wall-bounded flow. *J. Fluid Mech.* **757**, 888–907.
SUN, J., MAHRT, L., NAPPO, C. & LENSCHOW, D.H. 2015 Wind and temperature oscillations generated by wave–turbulence interactions in the stably stratified boundary layer. *J. Atmos. Sci.* **72** (4), 1484–1503.
TAYLOR, G.I. 1938 The spectrum of turbulence. *Proc. R. Soc. Lond.* A *Math. Phys. Sci.* **164** (919), 476–490.
TERRADELLAS, E., SOLER, M.R., FERRERES, E. & BRAVO, M. 2005 Analysis of oscillations in the stable atmospheric boundary layer using wavelet methods. *Boundary-Layer Meteorol.* **114** (3), 489–518.
TINNEY, C.E., COIFFET, F., DELVILLE, J., HALL, A.M., JORDAN, P. & GLAUSER, M.N. 2006 On spectral linear stochastic estimation. *Exp. Fluids* **41**, 763–775.
TOMKINS, C.D. & ADRIAN, R.J. 2003 Spanwise structure and scale growth in turbulent boundary layers. *J. Fluid Mech.* **490**, 37–74.
TOWNSEND, A.A.R. 1976 *The Structure of Turbulent Shear Flow*. Cambridge University Press.
WANG, G., GU, H. & ZHENG, X. 2020 Large scale structures of turbulent flows in the atmospheric surface layer with and without sand. *Phys. Fluids* **32** (10), 106604.
WANG, G. & ZHENG, X. 2016 Very large scale motions in the atmospheric surface layer: a field investigation. *J. Fluid Mech.* **802**, 464–489.
WARK, C.E. & NAGIB, H.M. 1991 Experimental investigation of coherent structures in turbulent boundary layers. *J. Fluid Mech.* **230**, 183–208.
YOON, M., HWANG, J., YANG, J. & SUNG, H.J. 2020 Wall-attached structures of streamwise velocity fluctuations in an adverse-pressure-gradient turbulent boundary layer. *J. Fluid Mech.* **885**, A12.
ZHANG, Y., HU, R. & ZHENG, X. 2018 Large-scale coherent structures of suspended dust concentration in the neutral atmospheric surface layer: a large-eddy simulation study. *Phys. Fluids* **30** (4), 046601.
ZHAO, L.H., ANDERSSON, H.I. & GILLISSEN, J.J.J. 2010 Turbulence modulation and drag reduction by spherical particles. *Phys. Fluids* **22** (8), 081702.